Disruption of kilometre-sized asteroids by energetic collisions

E. Asphaug*, S. J. Ostro†, R. S. Hudson‡, D. J. Scheeres§ & W. Benz‖

* *Department of Earth Sciences, University of California, Santa Cruz, California 95064, USA*
† *NASA Jet Propulsion Laboratory 300-233, Pasadena, California 91109-8099, USA*
‡ *School of Electrical Engineering and Computer Science, Washington State University, Pullman, Washington 99164-2752, USA*
§ *Department of Aerospace Engineering and Engineering Mechanics, Iowa State University, Ames, Iowa 50011-3231, USA*
‖ *Physikalisches Institut, Universität Bern, Sidlerstrasse 5, CH-3012 Bern, Switzerland*

Recent numerical studies[1–5] suggest that 'rubble-pile' asteroids (gravitationally bound aggregates of collisional debris) are common in the Solar System, and that self-gravitation may equal or exceed material cohesion for planetary bodies as small as several hundred metres. Because analytical scaling relations for impact cratering and disruption[6–8] do not extend to this size regime, where gravity and material strength are both important, detailed simulations are needed to predict how small asteroids evolve through impact, and also to ascertain whether powerful explosions offer a viable defence against bodies headed for a collision with Earth. Here we present simulations, using a smooth-particle hydrodynamics code[9], of energetic impacts into small planetary bodies with internal structure ranging from solid rock to porous aggregate. We find that the outcome of a collision is very sensitive to the configuration of pre-existing fractures and voids in the target. A porous asteroid (or one with deep regolith) damps the propagation of the shock wave from the impactor, sheltering the most distant regions, while greatly enhancing the local deposition of energy. Multiple-component asteroids (such as contact binaries) are also protected, because the shock wave cannot traverse the discontinuity between the components. We conclude that the first impact to significantly fragment an asteroid may determine its subsequent collisional evolution, and that internal structure will greatly influence attempts to disrupt or deflect an asteroid or comet headed towards Earth.

Target shape matters greatly during impacts[10], so for the exploratory simulations presented here we adopt a representative asteroid instead of a sphere: specifically, a three-dimensional shape model reconstructed[11] from radar images of the near-Earth asteroid 4769 Castalia. This peanut-shaped asteroid is 1.6 km in longest dimension, and is one of several Earth-crossing objects imaged in detail by radar[12]. Our three Castalia-shaped targets are made of (1) solid rock, (2) a pair of solid rocks separated by rubble, and (3) a 50% porous agglomeration of large boulders. These encompass several primary possible internal configurations of an asteroid. The material equation of state in each case is that of lunar gabbroic anorthosite[13,14], but substituting a specific density $\rho = 2.1\,\mathrm{g\,cm^{-3}}$ for the solid targets and $4.2\,\mathrm{g\,cm^{-2}}$ for the porous target, for a constant target mass of 1.2×10^{15} g. Elastic moduli and flaw-distribution parameters are derived from laboratory experiments in basalt[15,16]. (We do not suggest that near-Earth asteroids are actually composed of basalt or anorthosite, but until adequate material descriptions become available for better analogues, we adopt this laboratory-verified "standard rock" for simulations.) Our code, SPH3D (ref. 9), models shock propagation in elastic solids with a plastic yield criterion, and models explicit fracture and dynamic fragmentation under principal tension. The numerical resolution of each target is ~130,000 particles. Unless otherwise noted, each target is struck by an 8-m-radius, 5.8×10^9 g basalt sphere ($\rho = 2.7\,\mathrm{g\,cm^{-3}}$) at $5\,\mathrm{km\,s^{-1}}$. This speed is typical of asteroid collisions[17] in the main belt, although for Earth-crossing objects a somewhat higher nominal impact speed is appropriate. These impacts are equivalent in energy to the 17 kiloton Hiroshima bomb. The mechanical efficiency of an impact is considerably greater than that of an explosion, however, and the effect of nuclear weapons on asteroids must be studied separately.

This impactor barely exceeds the disruption threshold for the non-porous intact target (Fig. 1). A ~500-m-diameter damaged region forms, and distant fissures break the target into disconnected halves plus smaller pieces. We say that 'disruption' results when an intact asteroid is fragmented into pieces none more massive than half the original target, and that 'dispersal' results when less than half the original target's mass remains gravitationally bound following the collision. A rubble-pile forms when disruption greatly exceeds dispersal. Only ~10% of the target mass exceeds the nominal $\sim 40\,\mathrm{cm\,s^{-1}}$ escape velocity in this instance, so this event is not dispersive. For an irregular, rapidly-rotating asteroid like Castalia (period = 4 h), a detailed dynamical analysis is required to obtain the exact percentage. The impact imparts an impulse $\Delta v \sim 7\,\mathrm{cm\,s^{-1}}$ to the non-escaping fraction's centre of mass. Widespread surface fractures shown in Fig. 1 might become surface grooves such as those seen on the martian satellite Phobos and on

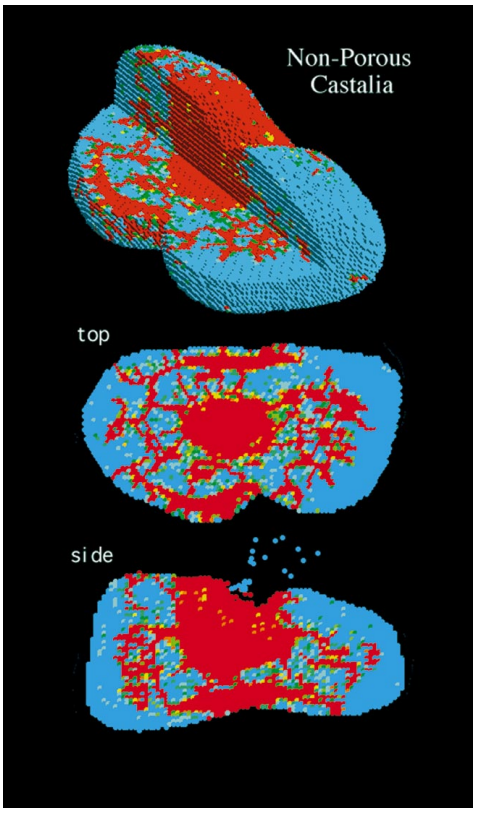

Figure 1 An initially intact Castalia (1.6 km longest dimension) seen 0.3 s after impact by an 8-m-radius basalt sphere at $5\,\mathrm{km\,s^{-1}}$. The energy of this impact is equivalent to the Hiroshima explosion. Blue is unfractured rock; red is fully damaged rock, incapable of supporting tensile or shear stress. The shock wave has by this time crossed the asteroid twice, and has dissipated below the fracture threshold. Full hydrodynamic and dynamical evolution of the evolving crater bowl and the mobilized fragments would take hours of real time, and has not been modelled. Thin slices through the target centre are also shown: blue ejected particles in the side view are pieces of the impactor, and will escape. The non-escaping fraction (~90%) of the asteroid receives a Δv of $\sim 7\,\mathrm{cm\,s^{-1}}$.

main-belt asteroids Gaspra and Ida[18–21]. The diameter of the fully damaged region is the same size as the crater diameter predicted by gravity scaling[22]—that is, if only gravity (and not strength) were a factor—implying that intact, rocky ~1-km bodies are near the size transition between strength- and gravity-dominance for large-scale cratering. Because strength has approximately equal influence here, ejecta velocities are greater than gravity scaling predicts, and ejecta deposited around this crater will be thin or absent.

The above simulation demonstrates that it is much easier to crack an intact ~1-km target in two than to disperse it. This could be an important mechanism for producing contact-binary forms among asteroids. Our next exploration is therefore the effect of an identical impactor striking one lobe of an initially binary Castalia, with intact lobes separated by ~20 m of fully damaged rubble (Fig. 2). In this case, due to impedance mismatch, shock energy is reflected from the discontinuity back into the struck lobe, which becomes utterly destroyed. The unstruck lobe suffers only minor damage. As before, ~10% of the target escapes; Δv is ~3 cm s^{-1}.

Porous targets can be similarly resistant to disruption, because shock wave propagation is hindered by irregularities and voids, resulting in localized energy deposition. However, a target which is porous and also strengthless might be comparatively easy to disperse. Figure 3 shows the aftermath of the same impactor striking the porous target, for comparison with Fig. 1; numerical resolution prevents us from separating the porous target into disconnected boulders, and hence the initial object is rigid. Almost all fracture damage (shown red) occurs within a ~500-m-diameter hemisphere centred on the impact point, with only minor damage far from the impact. More important differences are revealed by Fig. 4, which shows cross-sections of particle velocity and internal energy 1.2 s after projectile contact with the porous and non-porous targets. In the porous target, the shock dissipates rapidly with distance as work is done in the collapse of pores, and as scattering prevents coherent departure of shock energy from the impact zone. The resultant localized increase in particle speed and internal energy extends to a distance where the shock wave abruptly dies out. By comparison, the shock in the non-porous target (Fig. 1) is broadcast with few hindrances to the farthest reaches of the asteroid, leading to some disruption at great distance, and to lower energy deposition (kinetic or thermal) near the impact. More than half the porous target is accelerated beyond nominal escape velocity, and a *strengthless* rubble pile would be just barely dispersed by this event, with a Δv of ~14 cm s^{-1} applied to the remaining ~5×10^{14} g body. In our moderately-fragmented *rigid* porous body, however, only the damaged region can escape, which it does: no ejecta returns to fill the excavated crater or to form an ejecta blanket. As distal damage is hindered, a preponderance of large, pristine craters on an asteroid (such as 253 Mathilde[23]) might imply a porous yet coupled interior, or else internal heterogeneity sufficiently great to scatter the shock and localize energy deposition.

The impact vapour and melt in our porous target penetrates the surface, rather than being directed immediately outwards. This produces an ejecta pattern which is far from conical (compare the trajectory vectors in Fig. 4); subsurface thermal alteration and material mixing is likely[24]. A more precise equation of state, and a thermal conductivity model, is required in our code before quantitative predictions can be made about the degree of alteration and mixing, but the effect seems significant. A large meteoroid hitting a fine-grained porous target is less likely to result in such efficient vapour interpenetration, although laboratory experiments[25] show that energy deposition remains highly localized in these cases as well.

We conclude by examining scale-equivalence in impacts. Many

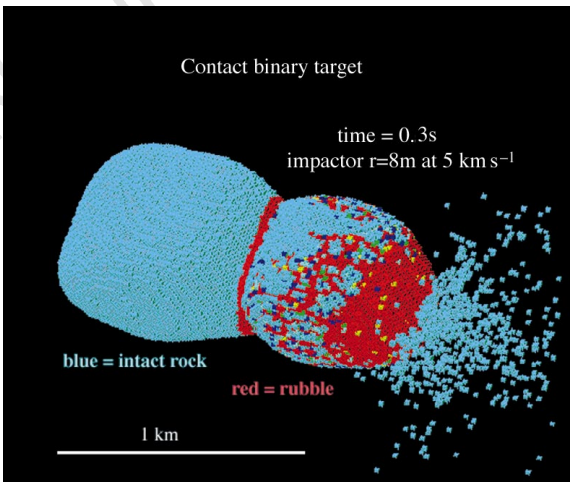

Figure 2 A contact-binary Castalia 0.3 s after impact by an 8-m-radius basalt sphere striking at 5 km s^{-1} on one end. The red band about the waist is pre-damaged, under-dense (1.7 g cm^{-3}) material which presents an impedance barrier for the shock, thereby reflecting its energy back into the struck lobe. While damage to the struck lobe is almost total, very little damage occurs in the distal lobe. The non-escaping fraction (~90%) of the asteroid receives a Δv of ~3 cm s^{-1}. The final configuration will consist of an intact kernel surrounded by debris.

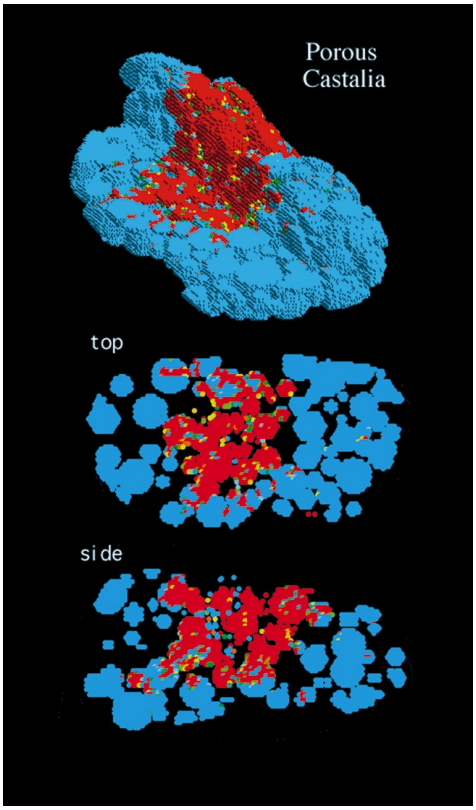

Figure 3 A 50% porous Castalia 0.3 s after impact by an 8-m-radius sphere at 5 km s^{-1}. The target is rigid, formed from connected spheres with sizes ranging from ~30 to ~100 m. (Numerical resolution prevents us from adding a plane of rubble between each contacting sphere, in the manner of Fig. 2.) Top and side views are thin-sections, with black representing void space initially present in the porous configuration, not to be confused with impact disaggregation. Final fracture damage (red) is shown for comparison with Fig. 1, and is restricted to the region near the impact. More than half this target is accelerated beyond escape velocity, although only the fractured region can actually be mobilized. A true, disconnected rubble pile would be dispersed by this collision, with a ~14 cm s^{-1} Δv applied to the ~5×10^{14} g non-escaping remainder.

aspects of a collision might be invariant to velocity provided that a 'coupling parameter'—essentially a hybrid between momentum (mv) and energy (mv^2)—is conserved[7]. Specifically, for solid rock targets, if $mv^{1.68}$ is held constant, the impact outcome should be the same. This relation has demonstrable merit in the case of hypervelocity cratering, at least in the gravity regime, provided that the impact speed is always much faster than the speed of sound in the target. However, our simulations show that for impact speeds much lower than this (~5 km s^{-1} in our non-porous targets and ~4 km s^{-1} in our porous target), such invariances are poor descriptors of collisional outcome[26]. Figure 5 compares the aftermath of a larger (20 m radius), slower (1 km s^{-1}) impactor, 'equivalent' to the 8 m, 5 km s^{-1} impactor of Fig. 1. In each case the asteroid cracks in two, but the predominant fractures for the slower projectile radiate from the impact, instead of propagating parallel beneath the surface. The greater amount of intermediate damage (shown yellow) and the smaller crater bowl (shown red) imply that impact disruption and cratering in the outer Solar System (where collision speeds are

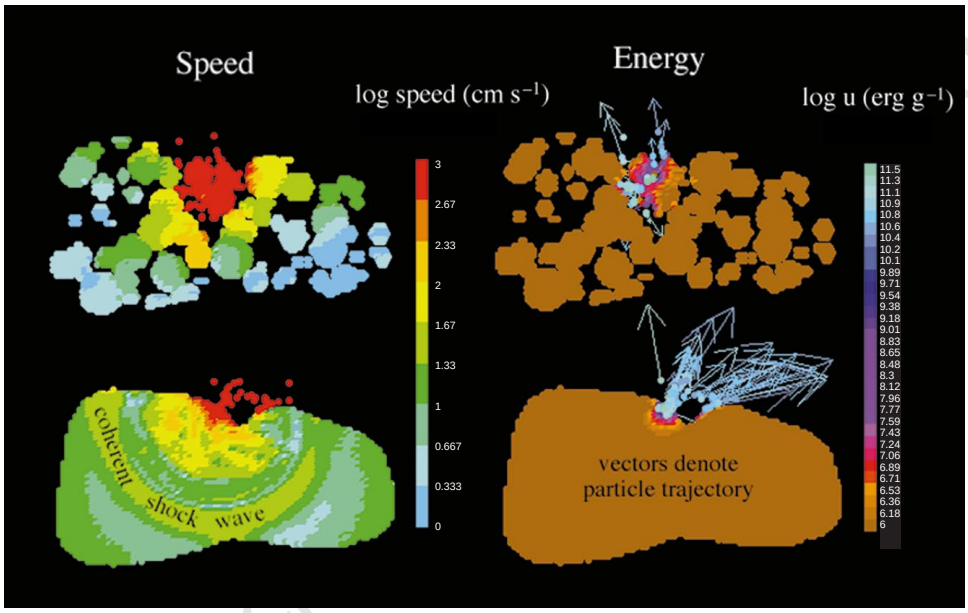

Figure 4 Effect of target porosity. Shown is a comparison of particle speed (left) and thermal energy (right) for the porous (top) and non-porous (bottom) targets. The target cross-sections are shown at $t = 0.12$ s. At this time in the simulation, the shock wave has progressed as a relatively coherent signal to the far surface of the non-porous target, carrying much of the impact energy away from the contact zone and creating the spallation fractures seen in Fig. 1. In the porous target, by contrast, the shock is scattered and its energy confined by the voids, resulting in a larger zone exceeding escape velocity (shown red and yellow) but lower intermediate velocities (shown green) and lower levels of distal disruption (Fig. 3). The entire damaged zone in the porous target exceeds escape velocity, and none of the far surface exceeds a few millimetres per second. The result will be a crater without an ejecta blanket, and minor seismic degradation in the distal regions of the target. Arrows in the energy plot indicate particle velocity, and show the dramatic effect of projectile interpenetration on ejecta trajectory.

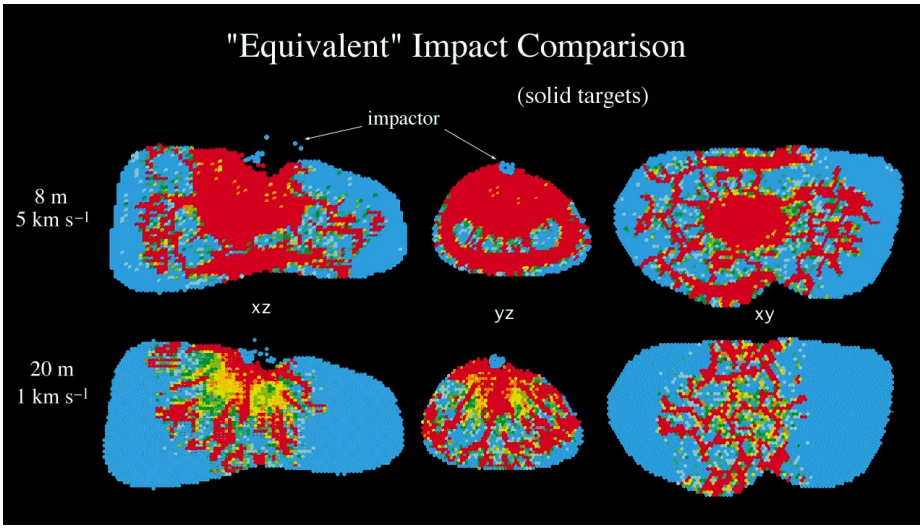

Figure 5 Effect of projectile size and speed. Shown is a comparison of fracture damage in the solid, non-porous Castalia for the original 8 m, 5 km s^{-1} projectile (top) versus a scale-equivalent 20 m, 1-km s^{-1} projectile striking at the same point. Although gross bulk aftermaths are the same (the target breaks in two, for instance), the surface-bounded spallation of the hypervelocity case (fractures propagating sub-parallel to the surface) is replaced by radial fissuring in the subsonic impact (fractures radiating from the impact point), and the crater diameter in the subsonic impact is considerably smaller. Twice as much material (25%) is accelerated to escaping speed by the slower, larger impactor. The remainder which does not escape receives an impulse $\Delta v \sim 7$ cm s^{-1}.

typically slower than $\sim 1\,\mathrm{km\,s^{-1}}$) might differ significantly from what is assumed by current modelling efforts[27]. The expected equation-of-state differences among small bodies (ice versus rock, for instance) presents another dimension of study; having recently adapted our code for massively parallel architectures (K. M. Olson and E.A, manuscript in preparation), we are now ready to perform a more comprehensive analysis.

The exploratory simulations presented here suggest that when a young, non-porous asteroid (if such exist) suffers extensive impact damage, the resulting fracture pattern largely defines the asteroid's response to future impacts. The stochastic nature of collisions implies that small asteroid interiors may be as diverse as their shapes and spin states. Detailed numerical simulations of impacts, using accurate shape models and rheologies, could shed light on how asteroid collisional response depends on internal configuration and shape, and hence on how planetesimals evolve. Detailed simulations are also required before one can predict the quantitative effects of nuclear explosions on Earth-crossing comets and asteroids, either for hazard mitigation[28] through disruption and deflection, or for resource exploitation[29]. Such predictions would require detailed reconnaissance concerning the composition and internal structure of the targeted object. □

Received 4 February; accepted 18 March 1998.

1. Asphaug, E. & Melosh, H. J. The Stickney impact of Phobos: A dynamical model. *Icarus* **101,** 144–164 (1993).
2. Asphaug, E. *et al.* Mechanical and geological effects of impact cratering on Ida. *Icarus* **120,** 158–184 (1996).
3. Nolan, M. C., Asphaug, E., Melosh, H. J. & Greenberg, R. Impact craters on asteroids: Does strength or gravity control their size? *Icarus* **124,** 359–371 (1996).
4. Love, S. J. & Ahrens, T. J. Catastrophic impacts on gravity dominated asteroids. *Icarus* **124,** 141–155 (1996).
5. Melosh, H. J. & Ryan, E. V. Asteroids: Shattered but not dispersed. *Icarus* **129,** 562–564 (1997).
6. Housen, K. R., Schmidt, R. M. & Holsapple, K. A. Crater ejecta scaling laws: Fundamental forms based on dimensional analysis. *J. Geophys. Res.* **88,** 2485–2499 (1983).
7. Holsapple, K. A. & Schmidt, R. M. Point source solutions and coupling parameters in cratering mechanics. *J. Geophys. Res.* **92,** 6350–6376 (1987).
8. Housen, K. R. & Holsapple, K. A. On the fragmentation of asteroids and planetary satellites. *Icarus* **84,** 226–253 (1990).
9. Benz, W. & Asphaug, E. Simulations of brittle solids using smooth particle hydrodynamics. *Comput. Phys. Commun.* **87,** 253–265 (1995).
10. Asphaug, E. *et al.* Mechanical and geological effects of impact cratering on Ida. *Icarus* **120,** 158–184 (1996).
11. Hudson, R. S. & Ostro, S. J. Shape of asteroid 4769 Castalia (1989 PB) from inversion of radar images. *Science* **263,** 940–943 (1994).
12. Ostro, S. J. *et al.* Asteroid radar astrometry. *Astron. J.* **102,** 1490–1502 (1991).
13. Ahrens, T. J. & O'Keefe, J. D. in *Impact and Explosion Cratering* (eds Roddy, D. J., Pepin, R. O. & Merrill, R. B.) 639–656 (Pergamon, New York, 1977).
14. Tillotson, J. H. Metallic equations of state for hypervelocity impact. (General Atomic Report GA-3216, San Diego, 1962).
15. Nakamura, A. & Fujiwara, A. Velocity distribution of fragments formed in a simulated collisional disruption. *Icarus* **92,** 132–146 (1991).
16. Benz, W. & Asphaug, E. Simulations of brittle solids using smooth particle hydrodynamics. *Comput. Phys. Commun.* **87,** 253–265 (1995).
17. Bottke, W. F., Nolan, M. C., Greenberg, R. & Kolvoord, R. A. Velocity distributions among colliding asteroids. *Icarus* **107,** 255–268 (1994).
18. Belton, M. J. S. *et al.* Galileo encounter with 951 Gaspra—First pictures of an asteroid. *Science* **257,** 1647–1652 (1992).
19. Belton, M. J. S. *et al.* Galileo's encounter with 243 Ida: An overview of the imaging experiment. *Icarus* **120,** 1–19 (1996).
20. Asphaug, E. & Melosh, H. J. The Stickney impact of Phobos: A dynamical model. *Icarus* **101,** 144–164 (1993).
21. Asphaug, E. *et al.* Mechanical and geological effects of impact cratering on Ida. *Icarus* **120,** 158–184 (1996).
22. Housen, K. R., Schmidt, R. M. & Holsapple, K. A. Crater ejecta scaling laws: Fundamental forms based on dimensional analysis. *J. Geophys. Res.* **88,** 2485–2499 (1983).
23. Veverka, J. *et al.* NEAR's flyby of 253 Mathilde: Images of a C asteroid. *Science* **278,** 2109–2112 (1997).
24. Asphaug, E. *et al.* Impact evolution of icy regoliths. *Lunar Planet. Sci. Conf. (Abstr.)* **XXVIII,** 63–64 (1997).
25. Love, S. G., Hörz, F. & Brownlee, D. E. Target porosity effects in impact cratering and collisional disruption. *Icarus* **105,** 216–224 (1993).
26. Fujiwara, A., Cerroni, P., Davis, D. R., Ryan, E. V. & DiMartino, M. in *Asteroids II* (eds Binzel, R. P., Gehrels, T. & Matthews, A. S.) 240–265 (Univ. Arizona Press, Tucson, 1989).
27. Davis, D. R. & Farinella, P. Collisional evolution of Edgeworth-Kuiper Belt objects. *Icarus* **125,** 50–60 (1997).
28. Ahrens, T. J. & Harris, A. W. Deflection and fragmentation of near-Earth asteroids. *Nature* **360,** 429–433 (1992).
29. *Resources of Near-Earth Space* (eds Lewis, J. S., Matthews, M. S. & Guerrieri, M. L.) (Univ. Arizona Press, Tucson, 1993).

Acknowledgements. This work was supported by NASA's Planetary Geology and Geophysics Program.

Correspondence and requests for materials should be addressed to E.A. (e-mail: asphaug@earthsci.ucsc.edu).

Collective dynamics of 'small-world' networks

Duncan J. Watts* & Steven H. Strogatz

Department of Theoretical and Applied Mechanics, Kimball Hall, Cornell University, Ithaca, New York 14853, USA

Networks of coupled dynamical systems have been used to model biological oscillators[1–4], Josephson junction arrays[5,6], excitable media[7], neural networks[8–10], spatial games[11], genetic control networks[12] and many other self-organizing systems. Ordinarily, the connection topology is assumed to be either completely regular or completely random. But many biological, technological and social networks lie somewhere between these two extremes. Here we explore simple models of networks that can be tuned through this middle ground: regular networks 'rewired' to introduce increasing amounts of disorder. We find that these systems can be highly clustered, like regular lattices, yet have small characteristic path lengths, like random graphs. We call them 'small-world' networks, by analogy with the small-world phenomenon[13,14] (popularly known as six degrees of separation[15]). The neural network of the worm *Caenorhabditis elegans*, the power grid of the western United States, and the collaboration graph of film actors are shown to be small-world networks. Models of dynamical systems with small-world coupling display enhanced signal-propagation speed, computational power, and synchronizability. In particular, infectious diseases spread more easily in small-world networks than in regular lattices.

To interpolate between regular and random networks, we consider the following random rewiring procedure (Fig. 1). Starting from a ring lattice with n vertices and k edges per vertex, we rewire each edge at random with probability p. This construction allows us to 'tune' the graph between regularity ($p = 0$) and disorder ($p = 1$), and thereby to probe the intermediate region $0 < p < 1$, about which little is known.

We quantify the structural properties of these graphs by their characteristic path length $L(p)$ and clustering coefficient $C(p)$, as defined in Fig. 2 legend. Here $L(p)$ measures the typical separation between two vertices in the graph (a global property), whereas $C(p)$ measures the cliquishness of a typical neighbourhood (a local property). The networks of interest to us have many vertices with sparse connections, but not so sparse that the graph is in danger of becoming disconnected. Specifically, we require $n \gg k \gg \ln(n) \gg 1$, where $k \gg \ln(n)$ guarantees that a random graph will be connected[16]. In this regime, we find that $L \sim n/2k \gg 1$ and $C \sim 3/4$ as $p \to 0$, while $L \approx L_{\mathrm{random}} \sim \ln(n)/\ln(k)$ and $C \approx C_{\mathrm{random}} \sim k/n \ll 1$ as $p \to 1$. Thus the regular lattice at $p = 0$ is a highly clustered, large world where L grows linearly with n, whereas the random network at $p = 1$ is a poorly clustered, small world where L grows only logarithmically with n. These limiting cases might lead one to suspect that large C is always associated with large L, and small C with small L.

On the contrary, Fig. 2 reveals that there is a broad interval of p over which $L(p)$ is almost as small as L_{random} yet $C(p) \gg C_{\mathrm{random}}$. These small-world networks result from the immediate drop in $L(p)$ caused by the introduction of a few long-range edges. Such 'short cuts' connect vertices that would otherwise be much farther apart than L_{random}. For small p, each short cut has a highly nonlinear effect on L, contracting the distance not just between the pair of vertices that it connects, but between their immediate neighbourhoods, neighbourhoods of neighbourhoods and so on. By contrast, an edge

* Present address: Paul F. Lazarsfeld Center for the Social Sciences, Columbia University, 812 SIPA Building, 420 W118 St, New York, New York 10027, USA.